HHS Public Access

Author manuscript

J Magn Reson Imaging. Author manuscript; available in PMC 2018 July 01.

Published in final edited form as:

J Magn Reson Imaging. 2017 July ; 46(1): 102–114. doi:10.1002/jmri.25595.

Accelerated Dual-*Venc* 4D flow MRI for neurovascular applications

Susanne Schnell, PhD[1], **Sameer A. Ansari, MD-PhD**[1,2], **Can Wu, PhD**[1,3], **Julio Garcia, PhD**[1,4], **Ian G Murphy, MD**[1], **Ozair A. Rahman, MD**[1], **Amir A. Rahsepar, MD**[1], **Maria Aristova**[1], **Jeremy D Collins, MD**[1], **James C Carr, MD**[1], and **Michael Markl, PhD**[1,2]

[1]Department of Radiology, Feinberg School of Medicine, Northwestern University, Chicago, USA

[2]Department of Neurosurgery, Northwestern University, Chicago, USA

[3]Department of Biomedical Engineering, McCormick School of Engineering, Northwestern University, Chicago, USA

[4]Department of Cardiac Sciences - Stephenson Cardiac Imaging Centre, Cumming School of Medicine, University of Calgary, Calgary, CAN

Abstract

Purpose—To improve velocity–to-noise ratio (VNR) and dynamic velocity range at 4D flow MRI by using dual-velocity encoding (dual-*venc*) with *k-t* GRAPPA acceleration.

Materials and Methods—A dual-*venc* 4D flow MRI sequence with *k-t* GRAPPA acceleration was developed using a shared reference scan followed by three-directional low- and high-*venc* scans (TR/TE/FA=6.1ms/3.4ms/15°, temporal/spatial resolution=43.0ms/1.2×1.2×1.2mm^3). The high-*venc* data was used to correct for aliasing in the low-*venc* data, resulting in a single dataset with the favorable VNR of the low-*venc* but without velocity aliasing. The sequence was validated at a 3 Tesla MRI Scanner in phantom experiments and applied in 16 volunteers to investigate its feasibility for assessing intracranial hemodynamics (net flow and peak velocity) at the major intracranial vessels. In addition, image quality and image noise was assessed in the in-vivo acquisitions.

Results—All 4D flow MRI scans were acquired successfully with an acquisition time of 20±4min. The shared reference scan reduced the total acquisition time by 12.5% compared to two separate scans. Phantom experiments showed 51.4% reduced noise for dual-*venc* compared to high-*venc* and an excellent agreement of velocities (ρ=0.8, p<0.001). The volunteer data showed decreased noise in dual-*venc* data (54.6% lower) compared to high-*venc*, and improved image quality, as graded by two observers: less artifacts (P<0.0001), improved vessel conspicuity (P<0.0001), and reduced noise (P<0.0001).

Conclusion—Dual-*venc* 4D flow MRI exhibits the superior VNR of the low-*venc* acquisition and reliably incorporates low- and high-velocity fields simultaneously. In-vitro and in-vivo data demonstrate improved flow visualization, image quality and image noise.

Address for Correspondence: Susanne Schnell, Ph.D., Department of Radiology, Northwestern University, 737 N. Michigan Avenue Suite 1600, Chicago, Illinois 60611, USA, susanne.schnell@northwestern.edu.

Keywords

4D flow MRI; dual *venc*; intracranial 4D flow MRI; PC-MRI; *k-t* GRAPPA

Introduction

4D flow MRI allows for the in-vivo volumetric assessment of 3D cardiovascular blood flow, and has been successfully applied in several studies (1–11). However, current 4D flow MRI techniques to measure blood velocity (v) are based on a single pre-defined velocity sensitivity ($venc$), which is typically set above the expected maximum velocity. This single-*venc* acquisition results in either velocity aliasing for unexpected high blood flow velocities ($v > venc$) or high noise levels for slow flow ($v < venc$), since velocity noise (σ_v) is directly proportional to the adjusted $venc$ ($\sigma_v \sim venc$) (12). As a result, previous applications of 4D flow MRI were limited by its inability to fully capture the wide dynamic range of velocities often encountered.

For complete evaluation of cardiac and neurovascular flow, it is desirable to gain quantitative information on both lower and high blood flow velocities simultaneously, which can differ by an order of magnitude even in normal subjects (e.g. slow venous flow on the order of 10 cm/s versus peak systolic atrial velocities of 150 cm/s) (13). To address these limitations, low- and high-*venc* 4D flow MRI can be performed successively (dual-*venc*) in two separate acquisitions. The resulting non-aliased high-*venc* data can then be used for pixel-wise anti-aliasing of the low-*venc* data. Dual-*venc* 4D flow MRI could thus provide improved quantification of the entire velocity spectrum.

Previous studies have investigated dual-*venc* approaches based on multiple subsequent 4D flow MRI acquisitions with two or more *venc* values and post-processing methods (14–16), or have used five-point balanced flow encoding to reduce noise and aliasing in phase images (17). Alternatively, velocity encoding was varied for acquiring data points during systole or diastole (18). A very early implementation of dual-*venc* 2D PC-MRI with through-plane velocity encoding, three-point phase contrast imaging, was reported by Lee et al. (12). Another approach by Binter et al. (19) used multipoint velocity encoding with *k-t* undersampling in combination with Bayesian analysis to map mean and fluctuating velocity for a large dynamic range. This method was validated against 3D particle image velocimetry (20) and was validated in an in vitro flow phantom and tested in the aorta in healthy controls and two patients. In addition, the method was applied to simultaneously acquire arterial and venous blood flow velocities as well as cerebrospinal fluid flow in 2D slices (21). A limitation of this method is the extensive processing time of the Bayes framework for a 3D volume with multiple velocity encodings, which was stated to be about 8 hours per in vivo dataset on a conventional personal computer.

The aim of this study was to develop and test a fully integrated *k-t* accelerated dual-*venc* 4D flow MRI sequence (3D volume and 3-directional velocity encoding) with a shared reference scan for the acquisition of both low- and high-*venc* data; therefore, a single acquisition to achieve the dynamic range of high-*venc* and the noise of low-*venc* measurements.

Materials and Methods

Sequence Development

Gradient waveforms for this seven-point velocity encoding scheme were designed following the strategies of Bernstein et al to minimize TE (22). For simplicity, we will henceforth refer to dual-*venc* 4D flow MRI instead of seven-point velocity encoding. As shown in Figure 1, similar to standard PC-MRI, the first gradient echo was used to measure the common reference MR-signal phase $\Phi^{(ref)}$. In the following 6 TRs, velocity encoding gradients were applied along the 3 orthogonal directions ($i = x, y, z$) with the required change in first moment ΔM_1 in each direction for both low- and high-*venc*. Six sets of phase difference images (three-directional low- and high-*venc* data) were obtained by subtracting the reference MR-signal phase from the following six flow-sensitive MR-signal phases. To achieve minimum echo time, a "two-sided" velocity encoding strategy was used (22).

Velocity encoding was determined by the duration and amplitudes of bipolar gradients ($G_i^{(ref)}$, $G_i^{(\text{low-}venc)}$, $G_i^{(\text{high-}venc)}$) in the three orthogonal directions ($i = x, y, z$) and the corresponding first-order gradient moments. For a desired total change in the first-gradient moment $\Delta M_{1i}^{(\text{low-}venc)}$ and with symmetrically divided two-sided velocity encoding for the low-*venc* acquisition, the first-gradient moments for the reference and flow-sensitive low-*venc* scans are $-\Delta M_{1i}^{(\text{low-}venc)}/2$ and $+\Delta M_{1i}^{(\text{low-}venc)}/2$, respectively with:

$$\Delta M_1^{(\text{low}-\text{venc})} = \frac{\pi}{\gamma|\text{low}-\text{venc}|} \quad (1)$$

where γ is the gyromagnetic ratio. To reduce acquisition time, the reference scan was shared for high-*venc* data acquisition. The first-order gradient moments were efficiently distributed between the reference ($M_{1i}^{(ref)}$, $i = x, y, z$), low-*venc* ($M_{1i}^{(\text{low})}$), and high-*venc* ($M_{1i}^{(\text{high})}$) scans based on the following boundary conditions:

$$\text{low}-\text{venc}_i = \frac{\pi}{\gamma \Delta M_{1i}^{(\text{low}-\text{venc})}} = \frac{\pi}{\gamma (M_{1i}^{(\text{low}-\text{venc})} - M_{1i}^{(\text{ref})})} \quad (2)$$

$$\text{high}-\text{venc}_i = \frac{\pi}{\gamma \Delta M_{1i}^{(\text{high}-\text{venc})}} = \frac{\pi}{\gamma (M_{1i}^{(\text{high}-\text{venc})} - M_{1i}^{(\text{ref})})} \quad (3)$$

As a result, the first-gradient moment difference for the high-*venc* encoding gradients can be calculated as:

$$\Delta M_1^{(\text{high}-\text{venc})} + \frac{\Delta M_1^{(\text{low}-\text{venc})}}{2} = \frac{\pi}{\gamma|\text{high}-\text{venc}|} \quad (4)$$

$$\Delta M_1^{(\text{high}-\text{venc})} = \frac{\pi}{\gamma|\text{high}-\text{venc}|} - \frac{\pi}{2\gamma|\text{low}-\text{venc}|} \quad (5)$$

Blood flow velocities $v_{i,j}$ were then reconstructed by subtracting the reference phase $\Phi^{(ref)}$ from the following 6 flow-sensitive phases $\Phi_i^{(j)}$:

$$\Phi_i^{(j)} = \gamma v_{i,j} M_{1i}^{(j)}: \quad v_{i,j} = \frac{\Delta\Phi_i^{(j)}}{\gamma \Delta M_{1i}^{(j)}} = \frac{\Phi_i^{(j)} - \Phi_i^{(\text{ref})}}{\gamma (M_{1i}^{(j)} - M_{1i}^{(\text{ref})})} \quad (6)$$

where *j* = *low, high*.

Since the low-*venc* acquisition requires higher first-order gradient moments and thus longer TE, the gradient waveforms were optimized based on the low-*venc* acquisition and the same timing was used for the high-*venc* gradient waveforms.

Acceleration of the dual-*venc* 4D flow MRI sequence was achieved with the '*PEAK*-GRAPPA' technique - an extension of *k-t* GRAPPA (23,24). Briefly, *k-t* GRAPPA is characterized by a uniform reconstruction kernel geometry composing a smallest cell within a k_y-k_z-*t* data undersampling pattern. The kernel extends over *k-t* space and consists of several acquired source points and missing target points. Kernel size and geometry determine which data is used for coil weight estimation, which then are used to fit the missing lines in the undersampled k-space. In combination with temporal averaging of coil weights, it has been shown that this approach leads to superior results compared to conventional *k-t* GRAPPA (25). The *PEAK* algorithm was integrated into the scanner's reconstruction workflow. A previous study (26) evaluated accuracy of net flow and peak velocity in 4D flow MRI. The results showed that an optimal acceleration factor was R=5 with only minimal over- or underestimation of peak velocity or net flow.

Dual-venc Phase-Contrast Reconstruction

Background-phase offsets were corrected for the low- and high-*venc* acquisitions using the gradient's Maxwell terms, which were calculated online and corrected during image reconstruction (27). Subsequently, eddy-current correction was performed independently for the low- and high-*venc* acquisitions (28). The high-*venc* data was corrected for velocity aliasing ensuring correct velocity values. The fully automated velocity unwrappping is based on the assumption that adjacent velocities in temporal or slice direction should not differ by more than *venc* (29). In the following step, the dual-*venc* data was reconstructed by using the corrected high-*venc* scan as an estimator for regional velocities to correct for velocity aliasing (Figure 2) in the low-*venc* data, similar to strategies for the 3-point approach by Lee et al. (12) or the 5-point approach by Johnson et al. (17). High- vs. low-*venc* phase difference images $D_i = \Phi_i^{(\text{high})} - \Phi_i^{(\text{low})}$ were used to estimate the number of phase wraps for each velocity direction *i* = *x, y* and *z*. The number of phase wraps was determined using thresholds. Voxels with single and double aliasing would be above thresh_1= low-*venc* * 1.6 and below thresh_2 = low-*venc* * 2.4 and twice the adjusted low-*venc* was added or subtracted

to the aliased voxel depending on the sign of D_i. Triple and four times aliased voxels would be above thresh_3 = low-*venc* * 3.2 and below thresh_4== low-*venc* * 4.8 and four times the adjusted low-*venc* was added or subtracted to the low-venc voxel.

$$v_{\text{dual}} = \begin{cases} \text{thesh}_1 < D_i < \text{thresh}_2: & v_{\text{low}} + (2 * \text{low} - \text{venc}) \\ -\text{thresh}_2 < D_i < -\text{thresh}_1: & v_{\text{low}} - (2 * \text{low} - \text{venc}) \\ \text{thesh}_3 < D_i < \text{thresh}_4: & v_{\text{low}} + (4 * \text{low} - \text{venc}) \\ -\text{thresh}_4 < D_i < -\text{thresh}_3: & v_{\text{low}} - (4 * \text{low} - \text{venc}) \end{cases} \quad (7)$$

We chose thresholds in dependence of the *venc* within a “soft-margin” of ±20% of the factor to account for voxels within the limits of noise in the high-*venc*. All reconstructions were performed under the assumption that there was no more than four times velocity aliasing.

Phantom Experiments

The dual-*venc* MRI sequence with 3-directional velocity encoding (TR/TE/FA = 5ms/2.7ms/15°, temporal resolution = 70ms, low-*venc*/high-*venc* = 100/200 cm/s) was tested with a rotation phantom on a 3T MRI scanner (MAGNETOM Skyra, Siemens Medical Systems, Erlangen, Germany). In addition to the dual-*venc* encoding, two standard 2D PC-MRI scans were performed for comparison (scan 1: *venc* = 100 cm/s, TR/TE/FA = 5ms / 2.7ms / 15°, temporal resolution = 40 ms; scan 2: *venc* = 200 cm/s, TR/TE/FA = 4.8ms / 2.4 ms / 15°, temporal resolution = 38.4 ms). All data were acquired with identical spatial resolution of $1.6 \times 1.6 \times 8\ \text{mm}^3$. A scan time reduction of 12.5% compared to two separate acquisitions was expected.

The rotation phantom design and dimensions are illustrated in Figure 3. The phantom consisted of a canister that rotated at various angular speeds using pressurized air and a fan blade rotation mechanism. The container was filled with a contrast-enhanced agar-gelatin mixture and rotations were counted with a photomicrosensor mounted to the upper rim of the container. The rotation speed for this experiment was set to 4.5 revolution per second (rev/s), resulting in velocities ranging from 0 – 200 cm/s depending on distance from the center of the phantom (cyan line in Figure 5B).

Velocities were compared between high-, low-, and dual-*venc* acquisitions along a horizontal cross section through the center of the phantom. Velocity noise was estimated using the standard deviation of absolute velocities (σ_v = std ($|v|$)) in successive time frames over the entire rotation phantom and compared between the dual-*venc* and the standard 2D PC-MRI scans.

Healthy Volunteer Study

The study was approved by our Institutional Review Board, and informed consent was obtained from all subjects. All scans were performed using a 3T MRI system (MAGNETOM Skyra). Each subject underwent *k-t* accelerated dual-*venc* 4D flow MRI using ECG gating with the following scan parameters: low-/high-*venc* combination (44/100 cm/s (8 cases), 48/110 cm/s (5 cases), and 60/130 cm/s (3 cases)), *k-t* GRAPPA acceleration with R = 5 and 20 × 8 k_y-k_z reference lines, TR/TE/FA = 6.1 ± 0.1ms / 3.4 ± 0.1ms / 15°,

temporal/spatial resolution = 43.0 ± 0.5 ms / 1.2 × 1.2 × 1.2 mm^3. The average thickness of the 3D slab was 5.6 ± 3.7 mm, covering the Circle of Willis. The acquired number of cardiac time frames were dependent on the heart rate.

In-vivo Dual-*venc* 4D Flow Processing

Data analysis for all 16 subjects included noise masking, velocity anti-aliasing, and corrections for Maxwell terms and eddy currents (Matlab, The Mathworks, Boston, MA, USA) (27,28) as illustrated in Figure 4. The dual-*venc* data set was reconstructed from the preprocessed low and high-*venc* data as described earlier and shown in Figure 2. In addition, a PC-MR angiogram (PC-MRA, Figure 4) was calculated for all 4D flow MRI data (low-*venc*, high-*venc*, dual-*venc*) using the piecewise pseudo complex difference:

$$I_{PC-MRA} = \begin{cases} \mathrm{Mag}\sin\left(\frac{\pi|v|}{\mathrm{venc}}\right)|v| & \text{for} |v| < \frac{2}{3}\cdot\mathrm{venc} \\ \mathrm{Mag} & \text{otherwise} \end{cases} \quad (8)$$

where *Mag* represents the magnitude and $|v|$ the absolute velocity (8). From all three calculated 3D PC-MRA data sets the maximum intensity projections (MIP) were generated (Figure 4). The low-*venc* 3D PC-MRA was then used as basis for the segmentation of the main intracranial vessels (MIMICS, Materialise, Leuven, Belgium). Both the 3D segmentation and 4D flow MRI data were loaded into a 3D flow visualization package (EnSight, CEI, Apex, NC, USA). The 3D segmentation was employed to restrict velocities to the segmented arterial and venous vessel boundaries for 3D flow visualization and quantification (Figure 4). Color-coded peak systolic 3D streamlines emitted from the entire segmented volume were used to visualize arterial and venous cerebrovascular blood flow patterns.

Data Analysis

To quantitatively assess image quality, velocity noise was compared between the high-*venc*, low-*venc* and reconstructed dual-*venc* 4D flow MRI data by calculating the voxel-wise standard deviation of velocity over time for each direction in a static region of the brain. The regions of interest for static tissue were drawn manually for each data set.

In addition, a semi-quantitative image quality grading of the derived 3D PC-MRA data was independently performed by one experienced radiologist (IM, over 5 years of training) and one recent medical graduate (OR), both blinded to subject identity and scan information as well as to each other's results using the MIP of the 3D PC-MRA in axial and coronal views. The level of noise and artifact was separately graded on a 3-point scale (mild = 0, moderate = 1, severe = 2), as well as the ability to depict the following vessels (0 = not present, 1 = partly/incomplete, 2 = clear/complete): right and left internal carotid arteries (rICA, lICA), right and left middle cerebral arteries (rMCA, lMCA), right and left anterior cerebral arteries (rACA, lACA), right and left posterior cerebral arteries (rPCA, lPCA), right and left vertebral arteries (rVA, lVA), basilar artery (BA), right and left transverse sinus (rTS, rTS) as well as the straight and superior sagittal sinus (StrSin, SagSin).

Further, regional flow quantification (net flow and peak velocity) was performed in all major intracranial arteries and veins (rICA, lICA, rMCA, lMCA, rACA, lACA, rVA, lVA, BA) and veins (rTS, lTS, StrSin, SagSin) using analysis planes perpendicular to the vessel as illustrated on the right of Figure 4 (EnSight, CEI, Apex, NC, USA). Note that the same segmented vasculature mask was used for the quantification of the low-, high- and dual-*venc* data.

Statistics

Data were tested for normal distribution using the Schapiro-Wilk test. All continuous values are reported with mean ± standard deviation unless specified differently. Pearson correlation was performed to compare the net flow and peak velocity between high-*venc* and dual-*venc* and between low-*venc* and dual-*venc*. The correlation was considered significant with a P value < 0.05 and correlation quality is expressed with correlation coefficient *R*. In addition, Bland-Altman analysis was performed for peak velocity and net flow. 3D PC-MRA image quality grades were compared between the three data sets (high-, low- and dual-*venc*) using the Wilcoxon rank sum test. A grading result was considered significantly different between high-, low- and dual-*venc* for a $P < 0.05$. The inter-rater agreement was tested with linearly weighted Cohen's kappa statistics, and significance of quality differences between low-, high- and dual-*venc* was tested using the Wilcoxon rank sum test. The data analysis for this paper was generated using the Real Statistics Resource Pack software (Release 4.3, Copyright (2013 – 2015) Charles Zaiontz. www.real-statistics.com).

Results

Phantom Experiments

Dual-*venc* and standard 2D PC-MRI data were successfully acquired as shown in Figure 5 by equivalent velocities for high- and dual-*venc* acquisitions along a cross section of the axial cut-plane of the rotating phantom. The use of a single common reference scan reduced the total acquisition time by 12.5% compared to running two separate scans. A total of 7 TRs was needed to acquire one *k*-space line for dual-*venc* data compared to 8 TRs for two separate low and high-*venc* acquisitions. Dual-*venc* reconstruction was successfully implemented as shown in Figure 5 B and correlation analysis shown in Figure 5 C. As expected, the dual-*venc* sequence showed 51.4% lower noise than high-*venc*. Rotation phantom velocities for high- and dual-*venc* acquisitions were strongly correlated (2-tailed Spearman correlation, $\rho = 0.8$, $P < 0.001$).

Healthy Volunteer Studies

k-t accelerated dual-*venc* 4D flow MRI data was successfully acquired in all 16 subjects (n = 16, age = 36 ± 12, 7 females) with an average total acquisition time (TA) of 20.3 ± 4.3 min. *k-t* GRAPPA reconstruction was performed online directly upon completion of data acquisition and took on average 13.0 ± 5.5 min. An average of 16.5 ± 1.8 cardiac time frames (ranging from 13 to 20) were acquired, depending on the subject's heart rate. No motion artefacts from head movement were noticed.

Qualitative Results of the In-Vivo Acquisition

Figure 6 shows results of in-vivo dual-*venc* 4D flow MRI in a healthy volunteer. More coherent and compact streamlines (Figure 6 C as well as zoomed in panels D, E, F, G and H) for dual-*venc* compared to high-*venc* can clearly be appreciated (Figure 6 A vs. 6 C). In addition, no velocity aliasing artifacts in streamline visualization compared to low-*venc* were observed (Figure 6 B vs. C, and F). In addition, 3D PC-MRA MIPs for all three reconstructions are shown (Figure 7 A–C). As expected, the low-*venc* and dual-*venc* data demonstrated less noise, fewer artifacts and superior vessel depiction.

These observations were confirmed by qualitative grading as summarized in Table 1. The grading results of the two observers show that dual-*venc* 4D flow MRI expressed a similar degree of artifacts ($P_{low\_vs\_dual} = 0.1875$, $P_{high\_vs\_dual} < 0.0001$, $P_{high\_vs\_low} = 0.0067$) as well as the ability to depict vessels ($P_{low\_vs\_dual} = 0.3750$, $P_{high\_vs\_dual} < 0.0001$, $P_{high\_vs\_low} < 0.0001$) as the low-*venc* data, but was superior to the high-*venc* data, and expressed the least amount of noise ($P_{low\_vs\_dual} = 0.0156$, $P_{high\_vs\_dual} < 0.0001$, $P_{high\_vs\_low} < 0.0001$) compared to low- and high-*venc* data.

The inter-rater agreement (linearly weighted Cohen's Kappa) for noise was fair ($\kappa = 0.352$), for artifacts moderate ($\kappa = 0.56$) and for overall vessel depiction moderate ($\kappa = 0.49$).

Cerebrovascular Flow Quantification

Regional flow quantification demonstrated similar peak velocity at all arterial locations ($P = 0.952$) and lower peak velocities in the dual-*venc* acquisition at all venous locations ($P = 0.012$) when compared to high-*venc*. Pearson correlation analysis showed that peak velocities in the arteries derived from the dual-*venc* data correlated well with the high-*venc* data, but not as well with the low-*venc* data (Figure 8 A, $R_{HV} = 0.95$, $P_{HV\text{-}DV} < 0.0001$, $R_{LV} = 0.72$, $P_{LV\text{-}DV} < 0.0001$). Venous peak velocities resulted in higher correlation coefficients for low- versus dual-*venc* (Figure 8 B). Bland-Altman analysis (Figure 9, left panel) showed excellent agreement between high- and dual-venc acquisition (offset = 0.003 m/s, limits of agreement = [+0.16 −0.15].

Net flow analysis revealed significantly higher values for the arterial ($P < 0.0001$) and venous system (median $netFlow_{venous\_dual} = 2.43$ ml/cycle, median $netFlow_{venous\_high} = 2.27$ ml/cycle, $P < 0.0001$) for dual-*venc* compared with high-*venc* data (Supporting Figures S1 and S2). Both low- and high-*venc* derived net flow showed significant correlation to the dual-*venc* data. However, the high-*venc* derived net flow in arterial vessels showed better correlation to the dual-*venc* ($R_{HV} = 0.98$, $R_{LV}=0.87$, $P_{HV\text{-}DV} = P_{LV\text{-}DV} < 0.0001$, Figure 8 C). Net flow increased in venous areas in the low-*venc* data compared to the high-*venc*. Therefore the correlation dual- vs low-*venc* data was improved compared to the high-*venc* data ($R_{LV} = 0.99$, $R_{HV} = 0.97$, $P_{HV\text{-}DV}=P_{LV\text{-}DV} < 0.0001$, Figure 8C and D). The individual differences for all vessels between the high- versus dual-*venc* scan for peak velocity and net flow are shown in Supporting Figures S1 and S2 for the interested reader. Bland-Altman analysis (Figure 9, right panel) of high- versus dual-*venc* confirmed the underestimation of net flow of the high-*venc* acquisition with an offset of −0.162 ml/cycle and limits of agreement at +0.49 and −0.82 ml/cycle.

Velocity noise in high-*venc* data was 0.088 ± 0.024 m/s (7.74% of adjusted high-*venc*, range = 0.058 – 0.148 m/s) compared to the low-*venc* data with 0.040 ± 0.011 m/s (7.91% of adjusted low-*venc*, range = 0.026 – 0.069 m/s). This resulted in a noise for the dual-*venc* 4D flow MRI data of 3.51% of adjusted high-*venc* (0.040 ± 0.011 m/s). This corresponds to noise reduction of 54.6%, which is close to the expected theoretical noise reduction of 55.8% calculated from the *venc*-ratio.

Discussion

A fully integrated dual-*venc* 4D flow MRI sequence was developed and compared with single-*venc* 4D flow MRI in a rotation phantom experiment and in a healthy volunteer feasibility study. VNR could be increased by the ratio of high- to low-*venc* by using the high-*venc* to correct velocity wrapping in the low-*venc* images. Noise evaluation in the volunteers also corresponded with the high/low-*venc* ratio. This resulted in excellent correlation of net flow and peak velocity compared to the high-*venc* scan in arteries and the low-*venc* scan in veins. The implemented *PEAK*-GRAPPA acceleration allowed image acquisition within a time comparable to standard single-*venc* 4D flow MRI.

Increased VNR resulted in improved quality of the calculated PC-MRA, which could be confirmed by two blinded observers. Increased net flow for dual-*venc* versus high-*venc* in venous vessels reflects the improved dynamic velocity range of the dual-*venc* acquisition. The observed difference of net flow between high-*venc* and low/dual-*venc* can be explained with the higher noise in the high-*venc* scan. Slow velocities contributing to net flow especially in veins are not measured with the high-*venc* scan. Variation in peak velocity can be expected to be as high as velocity noise in the range of 8% of *venc*, which is 8–10 cm/s depending on adjusted *venc* (100, 110 and 130 cm/s). Differences between low- and dual-*venc* can be explained with the velocity aliasing in the low-*venc* data.

This dual-*venc* 4D flow MRI implementation is very similar to the three-point 2D PC-MRI implementation by Lee et al. (12) and shows similar results for VNR gain. Our implementation, however, acquires a time-resolved 3D volume slab and applies velocity encoding in three spatial directions representing the seven-point encoding strategy. As in the three-point implementation, there is an acquisition time increase compared to single-*venc* due to the additional number of phase encoding gradients. However, with the usage of *k-t* GRAPPA acceleration of R = 5 we could achieve similar scan times as with single velocity encoding.

In the study by Nett et al, two separately acquired single-*venc* PC-VIPR (vastly undersampled isotropic-voxel radial projection imaging) scans were combined in a post-processing step and studied with both phantom and healthy control experiments (14). The phantom results showed significant improvement of VNR efficiency by a factor of 2.88 with only 5% increase in scan time. Additionally, the authors demonstrated successful unwrapping of the low-*venc* when using 12% of the acquired high-*venc* data. In their in-vivo experiments, a reasonable compromise between accuracy and scan time was found when combining a low-*venc* scan of 80 cm/s with 25% of a high-*venc* scan of 160 cm/s. For a theoretical full implementation of the presented method this would mean 25% longer scan

time than for a single-*venc* PC-VIPR acquisition, which is similar in regards of scan time to our *k-t* GRAPPA accelerated fully implemented dual-*venc* 4D flow MRI sequence when compared to current single-*venc* implementations. The advantage of retrospectively combining two single-*venc* acquisitions is that a better temporal resolution can be achieved than with a fully implemented method. The disadvantage is that one must correct for bulk motion, varying heart beats and variation of temporal resolutions due to longer echo times for the stronger gradients of the low-*venc* scan. However, reducing the amount of acquired high-*venc* data could also benefit our fully implemented dual-*venc* method and even further reduce scan time in addition to *k-t* GRAPPA acceleration.

Similar to the study by Nett et al (14), the multi-*venc* study by Ha et al. (15) utilized post-processing methods to combine separately acquired 4D flow acquisitions with multiple *venc*s. In this study, the high-*venc* scan was not used to unwrap the low-*venc* scan, but so-called valid voxels from each scan were combined resulting in a multi-*venc* overlapped dataset. The combination of the datasets makes estimation of velocity noise impossible, since noise is typically determined in static tissue, which is in the low signal range and thus taken from the scan with the lowest *venc*. However, additional noise is introduced into the dataset if voxels are assembled from all measurements; the velocity noise estimation from the static regions therefore is invalid. In addition to the aforementioned issues with using separate acquisitions, this imposes unpredictable noise situations in areas of high flow. Scan time depends on the number of separately acquired 4D flow acquisitions, and therefore, would be at least 12.5% longer than the fully implemented dual-*venc* acquisition for two acquired *venc*s.

The five-point encoding strategy introduced by Johnson et al (17) also using PC-VIPR reported a 63% increase in VNR (corresponding to a 39% noise reduction compared to 55% in our implementation) with minimal 1% increase in scan time when acquired with acceleration. This strategy involved the addition of a flow-compensated measurement to four-point encoding. A velocity estimate is determined from all five points and velocity is determined using the four non-compensated measurements. The phase gets unwrapped before the velocity is computed by using the velocity estimate. Velocity noise is similar to the standard four-point encoding; however, resulting velocities are automatically unwrapped. In this method, the gain in dynamic range cannot be adjusted as it can be done with a true dual-*venc* implementation. Because the noise reduction is proportional to the two adjusted *vencs* in the fully implemented dual-*venc* approach, the gain of VNR in the five-point encoding strategy is lower.

For the five-point implementation by Johnson et al. (17) and for the post-processsing dual-*venc* study by Nett et al. (14) PC-VIPR was used to acquire 4D flow MRI data. VIPR is a high speed 4D flow MRI method and uses radial k-space sampling evenly spaced through a spherical volume each intersecting the origin of k-space. PC-VIPR allows higher volume coverage and spatial resolution as well as faster sampling of k-space. However, radial sampling methods can often introduce streak artefacts, because of the difficult handling of k-space trajectory errors. The advantage of using radial acquisition is that it has different spatial aliasing and artifact behavior than Cartesian sampling (streak artifacts instead of spatial aliasing and wrapping), which allows for highly undersampled acquisitions as it is

done in PC-VIPR. Another advantage is more flexible temporal view sharing since each line goes through central k-space. *PEAK*-GRAPPA on the other hand is easier to implement and applied for Cartesian k-space acquisition schemes. Both methods have been extensively validated. However, a thorough comparison of the methods in regards of flow quantification is still outstanding.

With Fourier velocity-encoding (FVE), a wide range of velocities can be encoded (30). With FVE the distribution of velocities within a pixel can be measured, rather than only the weighted average. In FVE, a series of e.g. 8 or 16 values of flow encoding steps is used and separated by constant increment of the first moment ΔM_1. The resulting hybrid spatial-velocity *k*-space is reconstructed with a discrete Fourier transform instead of a phase difference method. This yields a set of images for each pixel sensitive to velocity within a specific range. FVE has the advantage that by examining the zero velocity image the stationary tissue contribution to the signal for each pixel can be measured. However, in order to achieve precise velocity information within a reasonable scan time, there is a trade-off between spatial resolution, number of encoded spatial dimensions, or temporal resolution. The acquisition time penalty is the reason why FVE has found most applications with 1D pencil beam excitation imaging (31). Although it may be utilized to assess flow in the coronary arteries (32) which is intrinsically fast, it does not allow measurement of three-dimensional flow in a 3D volume. Wise et al (33) combined FVE with sparse sampling and a Bayesian technique of probability analysis, which allows sparse sampling and thus fast acquisition times. Binter et al used multipoint velocity encoding and combined it with the Bayesian approach with *k-t* undersampling methods, which allows mapping turbulence (19) within a reasonable scan time. This method provides an increase in accuracy and dynamic range, but its extensive processing time of the Bayes framework of (8 hours for a full aortic 3D dataset) is a limiting factor for in-vivo studies. One intracranial in-vivo application of Bayesian Multipoint Velocity-encoded MRI was reported to simultaneously quantify flow in the arterial and venous systems as well as CSF flow (21). However, this study employed only 2D slices and through-plane velocity encoding at pre-specified locations. Acquisition time was similar to standard 2D PC MR imaging; however, no noise comparison was provided.

In the variable velocity encoding strategy (4D-vPC) introduced by Swan et al (34) and extended in 3D by Nilsson et al (18), the *venc* is varied for all three directions over the cardiac cycle. The approach uses a standard balanced four-point velocity encoding scheme, but the bipolar gradient strengths were recalculated to correspond to a predefined *venc* in each heart phase while keeping the slope of the bipolar gradient pair constant. The velocity information in the 4D-vPC sequence is retrospectively corrected for *venc* variation after the acquisition. The acquisition time is similar to a standard four-point acquisition scheme. Noise estimation was performed in a rotating phantom and was similar to the noise of a standard four-point strategy with a fixed *venc* of the highest adjusted *venc* of the 4D-vPC. As expected, the in-vivo noise ratios showed large variations. However, when looking at streamline visualization, a clearer identification of flow patterns could be achieved during diastole compared to standard four-point encoding. This implementation of variable *venc* requires prior information of temporal velocity variation and length of systole. In contrast to

a fully implemented dual-*venc* sequence, both high and low velocities occurring during systole cannot be captured and thus low flow remains corrupted by noise.

A limitation of the dual-*venc* 4D flow MRI implementation presented here is that it requires prior knowledge of the highest potentially occurring velocity to adapt the high-*venc* accordingly and avoid velocity aliasing. However, the high-*venc* can be adjusted more flexibly than for the standard single-*venc* acquisition, since VNR is determined by the low-*venc* acquisition. The current implementation requires 7 TRs for both low- and high-*venc* data acquisitions, which results in 75% longer scan time than a single-*venc* acquisition as well as lower temporal resolution assuming the same number of *k*-space lines per cardiac cycle are used. These are limitations of the methods and can be an advantage or disadvantage depending on the application. For example, the resulting scan time would actually be shorter in applications where two 4D flow MRI scans at low- and high-*venc* are typically acquired, such as in the liver or brain, where both venous and arterial flow are of interest. Furthermore, for applications where only a single 4D flow MRI acquisition is typically performed, the gain in VNR and velocity range may be more important than a shorter scan time: for example, when investigating patients with aortic stenosis. A smaller field of view (smaller imaging volume) could also be offset by high spatial resolution and shorter scan times, which would be feasible in a limited volume of interest e.g. intracranial aneurysm. In addition, due to the low pulsatility (in comparison to the thoracic aorta), intracranial applications of dual-*venc* with lower temporal resolution seem feasible.

Another limitation of the implementation using the shared reference scan is the reduced temporal resolution. Typical 4D flow MRI studies in the brain as well as in the body use a temporal resolution of 40ms. We kept the temporal resolution in the similar range and used *PEAK*-GRAPPA to achieve similar scan times than for a single-*venc* acquisition. In fact, Bammer et al. (35) studied the effect of temporal resolution on blood flow quantification in the brain and demonstrated that 4D flow MRI is feasible for the measurement and visualization of blood flow in the major intracranial vessels with a required temporal resolution of <65ms.

Velocity noise was estimated using standard deviation over time to account for the spatial variation of image noise as a result of the *k*-*t* parallel imaging. The accurate estimation of regional noise would have required the acquisition of additional 'noise only' data (by setting the flip angle to zero), which could not be performed in the framework of our already lengthy imaging protocols. In addition, we performed a visual grading of image quality by two blinded and independent radiologists, which provided another measure of objectivity.

The inter-rater qualitative image quality grading agreement was only fair to moderate, indicating differences in the raters' definition of a high quality exam, which was probably influenced by differences in observer experience. The more experienced observer consistently rated image quality (superior vs inferior) to the less experienced observer. Despite the suboptimal agreement, both an experienced and inexperienced observer agreed that phase contrast angiograms from dual- and low-*venc* acquisitions were superior to the high-*venc*.

It should be noted that a more equitable comparison of single-*venc* versus dual-*venc* would include two successive high-*venc* acquisitions and averaging. As a result, acquisition time would be 12.5% longer than for dual-*venc* 4D flow MRI, but result in a SNR gain of 144%. For dual-*venc* 4D flow MRI, the SNR gain is proportional to *venc* and thus higher than averaging two serial scans (depending on the chosen low-/high-*venc* combination). Furthermore, since each individual high-*venc* acquisition cannot capture slow velocities below or at the noise level, these velocities can also not be recovered by averaging several high-*venc* acquisitions.

Further investigation of the dual-*venc* acquisition needs to be performed in future studies as the maximum VNR achievable remains limited by various factors. Specifically, as the low-*venc* is lowered, unwrapping becomes more sensitive to velocity noise in the high-*venc* acquisition and results in phase unwrapping errors when the high-*venc* image has errors from noise. In addition, a lot of data are omitted by not using the high-*venc* scan for any other purpose than unwrapping and there may be other information in the data we are not using for this presented approach. Furthermore, there are a couple of limitations in study design such as the small cohort size with only healthy volunteers for this feasibility study as well as the lack of an external validation study. We also did not acquire additional separate single-*venc* acquisitions to directly compare dual- with single-*venc* 4D flow MRI due to scan time limitations.

In conclusion, this study has elucidated the importance of dual velocity encoding to improve the velocity-to-noise ratio as well as quantification of fast arterial and slow venous flow with a single 4D flow MRI acquisition in the brain. The findings of this feasibility study show that *k-t* GRAPPA accelerated dual-*venc* 4D flow MRI can provide improved visualization and quantification of venous and arterial hemodynamics across a wide range of the velocity spectrum. Velocity noise was significantly reduced compared to standard single-*venc* implementations. Further work includes integration of the phase-unwrapping algorithms to the inline image reconstruction pipeline and undersampling methods for the high-*venc* portion. The optimized dual-*venc* 4D flow MRI sequence can be employed for improved measurement of in-vivo blood flow and may be particularly useful in settings requiring evaluation of both low- and high-velocities such intracranial, abdominal, or whole heart 4D flow MRI studies.

Supplementary Material

Refer to Web version on PubMed Central for supplementary material.

Acknowledgments

Grant Support: DFG SCHN 1170/1-1, SIR Foundation pilot study grant, AHA Predoctoral Fellowship 14PRE18370014, AHA Posdoctoral Fellowship 14POST18350019, AHA Grant-in-Aid 13GRNT17340018, AHA Scientist Development Grant 16SDG30420005, Radiological Society of North America Research Seed Grant RSD1207, and NHLBI R01HL115828.

References

1. Wu C, Schnell S, Markl M, Ansari SA. Combined DSA and 4D Flow Demonstrate Overt Alterations of Vascular Geometry and Hemodynamics in an Unusually Complex Cerebral AVM. Clinical neuroradiology. 2015
2. Wu C, Ansari SA, Honarmand AR, et al. Evaluation of 4D vascular flow and tissue perfusion in cerebral arteriovenous malformations: influence of Spetzler-Martin grade, clinical presentation, and AVM risk factors. AJNR American journal of neuroradiology. 2015; 36(6):1142–1149. [PubMed: 25721076]
3. Markl M, Wu C, Hurley MC, et al. Cerebral arteriovenous malformation: complex 3D hemodynamics and 3D blood flow alterations during staged embolization. Journal of magnetic resonance imaging : JMRI. 2013; 38(4):946–950. [PubMed: 24027116]
4. Schuchardt F, Schroeder L, Anastasopoulos C, et al. In vivo analysis of physiological 3D blood flow of cerebral veins. European radiology. 2015; 25(8):2371–2380. [PubMed: 25638218]
5. Harloff A, Zech T, Wegent F, Strecker C, Weiller C, Markl M. Comparison of blood flow velocity quantification by 4D flow MR imaging with ultrasound at the carotid bifurcation. AJNR American journal of neuroradiology. 2013; 34(7):1407–1413. [PubMed: 23413247]
6. Hope TA, Hope MD, Purcell DD, et al. Evaluation of intracranial stenoses and aneurysms with accelerated 4D flow. Magnetic resonance imaging. 2010; 28(1):41–46. [PubMed: 19577400]
7. Boussel L, Rayz V, Martin A, et al. Phase-contrast magnetic resonance imaging measurements in intracranial aneurysms in vivo of flow patterns, velocity fields, and wall shear stress: comparison with computational fluid dynamics. Magnetic resonance in medicine : official journal of the Society of Magnetic Resonance in Medicine / Society of Magnetic Resonance in Medicine. 2009; 61(2): 409–417.
8. Schnell S, Ansari SA, Vakil P, et al. Three-dimensional hemodynamics in intracranial aneurysms: influence of size and morphology. Journal of magnetic resonance imaging : JMRI. 2014; 39(1):120–131. [PubMed: 24151067]
9. Kecskemeti S, Johnson K, Wu Y, Mistretta C, Turski P, Wieben O. High resolution three-dimensional cine phase contrast MRI of small intracranial aneurysms using a stack of stars k-space trajectory. Journal of magnetic resonance imaging : JMRI. 2011
10. Isoda H, Ohkura Y, Kosugi T, et al. In vivo hemodynamic analysis of intracranial aneurysms obtained by magnetic resonance fluid dynamics (MRFD) based on time-resolved three-dimensional phase-contrast MRI. Neuroradiology. 2010; 52(10):921–928. [PubMed: 20012431]
11. Hollnagel DI, Summers PE, Poulikakos D, Kollias SS. Comparative velocity investigations in cerebral arteries and aneurysms: 3D phase-contrast MR angiography, laser Doppler velocimetry and computational fluid dynamics. NMR in biomedicine. 2009; 22(8):795–808. [PubMed: 19412933]
12. Lee AT, Pike GB, Pelc NJ. Three-point phase-contrast velocity measurements with increased velocity-to-noise ratio. Magnetic resonance in medicine : official journal of the Society of Magnetic Resonance in Medicine / Society of Magnetic Resonance in Medicine. 1995; 33(1):122–126.
13. Markl M, Harloff A, Bley TA, et al. Time-resolved 3D MR velocity mapping at 3T: improved navigator-gated assessment of vascular anatomy and blood flow. Journal of magnetic resonance imaging : JMRI. 2007; 25(4):824–831. [PubMed: 17345635]
14. Nett EJ, Johnson KM, Frydrychowicz A, et al. Four-dimensional phase contrast MRI with accelerated dual velocity encoding. Journal of magnetic resonance imaging : JMRI. 2012
15. Ha H, Kim GB, Kweon J, et al. Multi-VENC acquisition of four-dimensional phase-contrast MRI to improve precision of velocity field measurement. Magnetic resonance in medicine : official journal of the Society of Magnetic Resonance in Medicine / Society of Magnetic Resonance in Medicine. 2015
16. Callaghan FM, Kozor R, Sherrah AG, et al. Use of multi-velocity encoding 4D flow MRI to improve quantification of flow patterns in the aorta. Journal of magnetic resonance imaging : JMRI. 2015

17. Johnson KM, Markl M. Improved SNR in phase contrast velocimetry with five-point balanced flow encoding. Magnetic resonance in medicine : official journal of the Society of Magnetic Resonance in Medicine / Society of Magnetic Resonance in Medicine. 2010; 63(2):349–355.

18. Nilsson A, Bloch KM, Carlsson M, Heiberg E, Stahlberg F. Variable velocity encoding in a three-dimensional, three-directional phase contrast sequence: Evaluation in phantom and volunteers. Journal of magnetic resonance imaging : JMRI. 2012; 36(6):1450–1459. [PubMed: 23065951]

19. Binter C, Knobloch V, Manka R, Sigfridsson A, Kozerke S. Bayesian multipoint velocity encoding for concurrent flow and turbulence mapping. Magnetic resonance in medicine : official journal of the Society of Magnetic Resonance in Medicine / Society of Magnetic Resonance in Medicine. 2013; 69(5):1337–1345.

20. Knobloch V, Binter C, Gulan U, et al. Mapping mean and fluctuating velocities by Bayesian multipoint MR velocity encoding-validation against 3D particle tracking velocimetry. Magnetic resonance in medicine : official journal of the Society of Magnetic Resonance in Medicine / Society of Magnetic Resonance in Medicine. 2014; 71(4):1405–1415.

21. Knobloch V, Binter C, Kurtcuoglu V, Kozerke S. Arterial, venous, and cerebrospinal fluid flow: simultaneous assessment with Bayesian multipoint velocity-encoded MR imaging. Radiology. 2014; 270(2):566–573. [PubMed: 24471394]

22. Bernstein MA, Shimakawa A, Pelc NJ. Minimizing TE in moment-nulled or flow-encoded two- and three-dimensional gradient-echo imaging. Journal of magnetic resonance imaging : JMRI. 1992; 2(5):583–588. [PubMed: 1392252]

23. Huang F, Akao J, Vijayakumar S, Duensing GR, Limkeman M. k-t GRAPPA: a k-space implementation for dynamic MRI with high reduction factor. Magnetic resonance in medicine : official journal of the Society of Magnetic Resonance in Medicine / Society of Magnetic Resonance in Medicine. 2005; 54(5):1172–1184.

24. Jung B, Ullmann P, Honal M, Bauer S, Hennig J, Markl M. Parallel MRI with extended and averaged GRAPPA kernels (PEAK-GRAPPA): optimized spatiotemporal dynamic imaging. Journal of magnetic resonance imaging : JMRI. 2008; 28(5):1226–1232. [PubMed: 18972331]

25. Jung B, Stalder AF, Bauer S, Markl M. On the undersampling strategies to accelerate time-resolved 3D imaging using k-t-GRAPPA. Magnetic resonance in medicine : official journal of the Society of Magnetic Resonance in Medicine / Society of Magnetic Resonance in Medicine. 2011; 66(4): 966–975.

26. Schnell S, Markl M, Entezari P, et al. k-t GRAPPA accelerated four-dimensional flow MRI in the aorta: effect on scan time, image quality, and quantification of flow and wall shear stress. Magnetic resonance in medicine : official journal of the Society of Magnetic Resonance in Medicine / Society of Magnetic Resonance in Medicine. 2014; 72(2):522–533.

27. Bernstein MA, Zhou XJ, Polzin JA, et al. Concomitant gradient terms in phase contrast MR: analysis and correction. Magnetic resonance in medicine : official journal of the Society of Magnetic Resonance in Medicine / Society of Magnetic Resonance in Medicine. 1998; 39(2):300–308.

28. Walker PG, Cranney GB, Scheidegger MB, Waseleski G, Pohost GM, Yoganathan AP. Semiautomated method for noise reduction and background phase error correction in MR phase velocity data. Journal of magnetic resonance imaging : JMRI. 1993; 3(3):521–530. [PubMed: 8324312]

29. Bock, JK., Hennig, J., Markl, M. Optimized pre-processing of time-resolved 2D and 3D Phase Contrast MRI data. Proceedings Scientific Meeting ISMRM; Berlin. 2007. p. 3138

30. Moran PR. A flow velocity zeugmatographic interlace for NMR imaging in humans. Magnetic resonance imaging. 1982; 1(4):197–203. [PubMed: 6927206]

31. Hardy CJ, Bolster BD Jr, McVeigh ER, Iben IE, Zerhouni EA. Pencil excitation with interleaved fourier velocity encoding: NMR measurement of aortic distensibility. Magnetic resonance in medicine : official journal of the Society of Magnetic Resonance in Medicine / Society of Magnetic Resonance in Medicine. 1996; 35(6):814–819.

32. Macgowan CK, Liu GK, van Amerom JF, Sussman MS, Wright GA. Self-gated Fourier velocity encoding. Magnetic resonance imaging. 2010; 28(1):95–102. [PubMed: 19553052]

33. Wise RG, Newling B, Gates AR, Xing D, Carpenter TA, Hall LD. Measurement of pulsatile flow using MRI and a Bayesian technique of probability analysis. Magn Reson Imaging. 1996; 14(2): 173–185. [PubMed: 8847973]

34. Swan JS, Weber DM, Grist TM, Wojtowycz MM, Korosec FR, Mistretta CA. Peripheral MR angiography with variable velocity encoding. Work in progress. Radiology. 1992; 184(3):813–817. [PubMed: 1509072]

35. Bammer R, Hope TA, Aksoy M, Alley MT. Time-resolved 3D quantitative flow MRI of the major intracranial vessels: initial experience and comparative evaluation at 1.5T and 3.0T in combination with parallel imaging. Magnetic resonance in medicine : official journal of the Society of Magnetic Resonance in Medicine / Society of Magnetic Resonance in Medicine. 2007; 57(1):127–140.

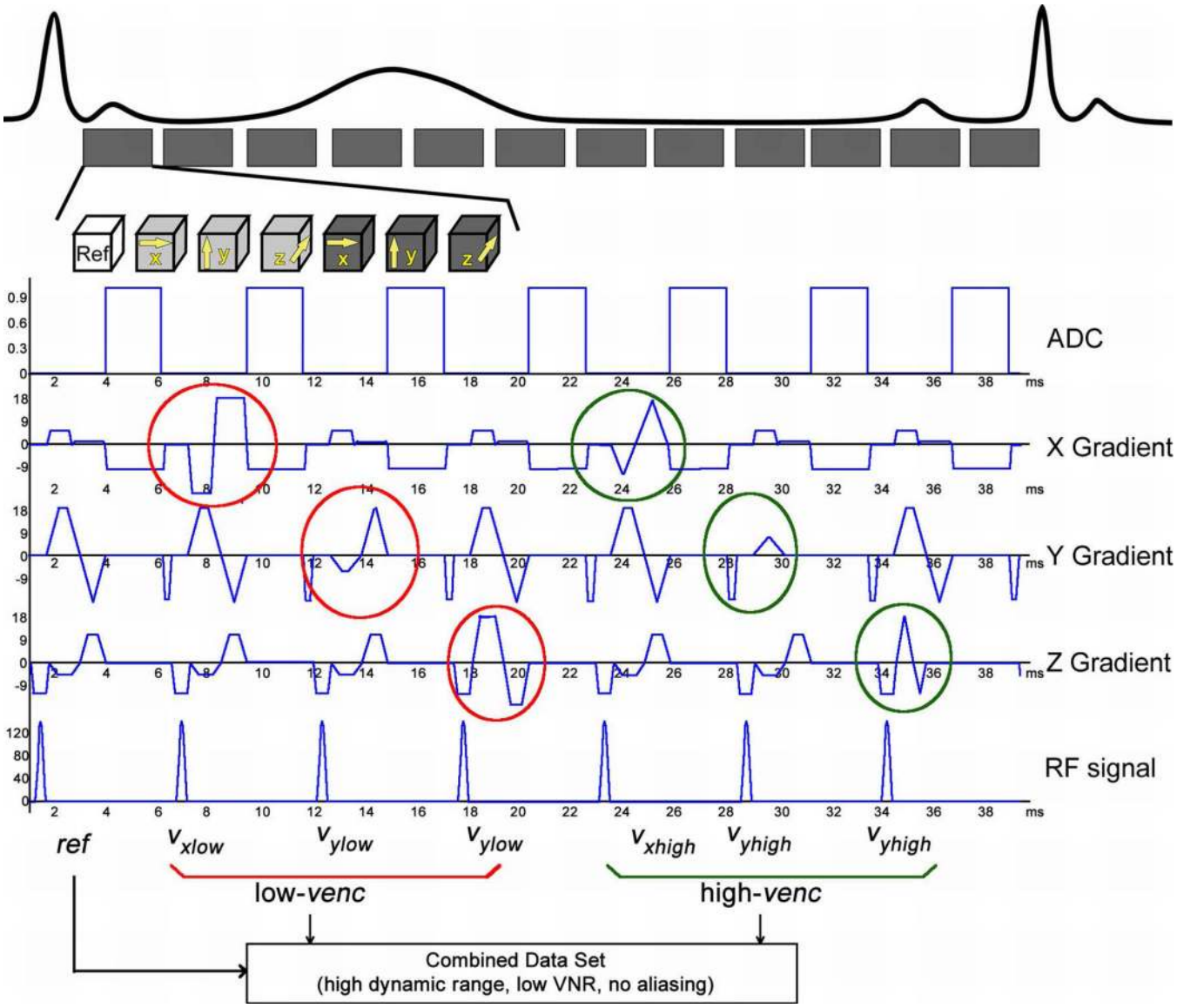

Figure 1.

Dual-*venc* PC-MRI sequence with a shared reference scan (ref) followed by low-*venc* and high-*venc* velocity encoding in three orthogonal directions (*x, y*, and *z*). A combined data set for each cardiac time frame was reconstructed utilizing the high VNR of the low-*venc* scan and the high-*venc* data for anti-aliasing. *Note that a total of 7 TRs is needed to acquire one k-space line for dual-*venc *data compared to 8TRs that would be required for two separate low- and high-*venc *acquisitions.*

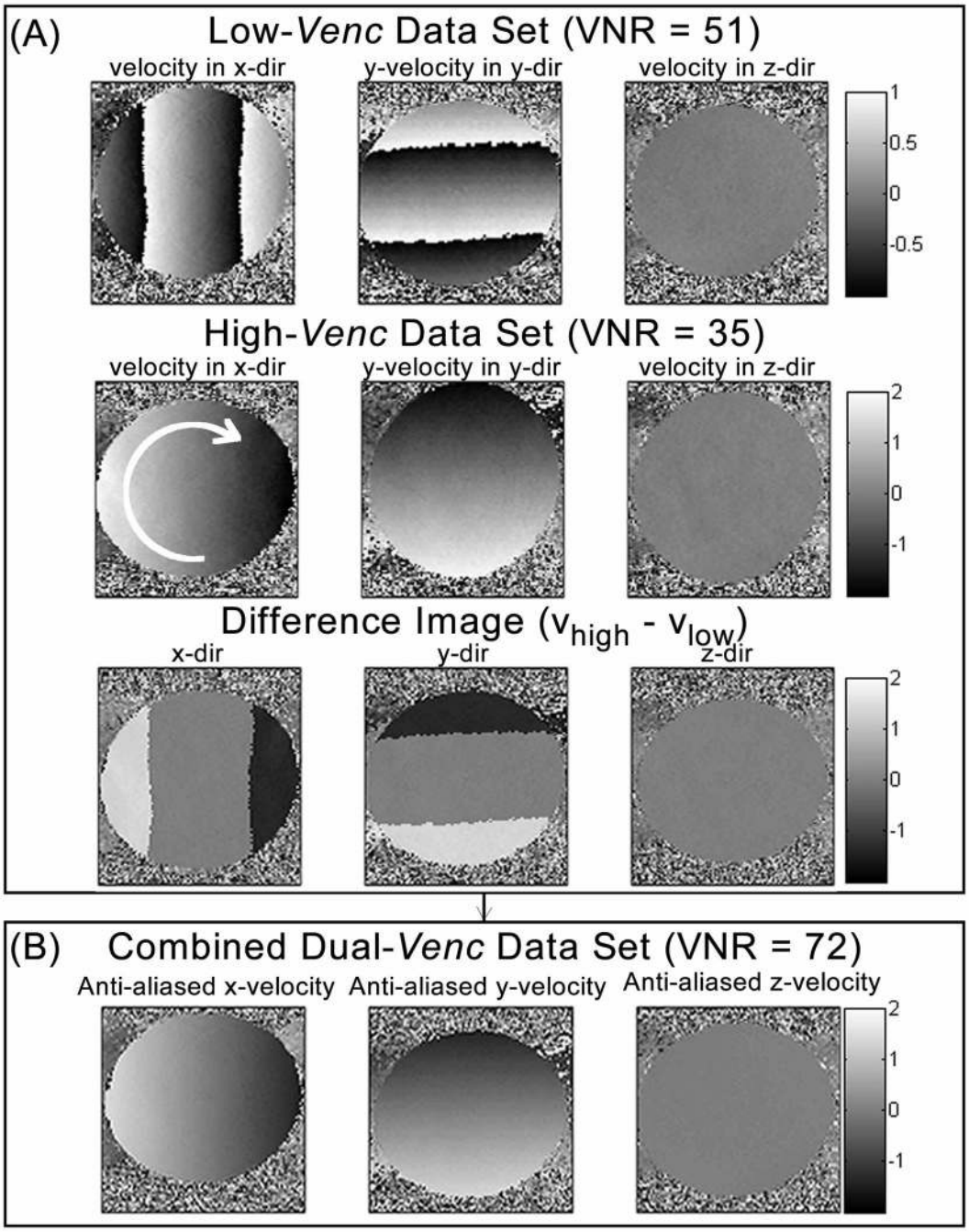

Figure 2.

Dual-*venc* phase contrast reconstruction using the low-*venc* scan (top row in (A)) as basis image and correcting the aliased voxels by comparing with the high-*venc* scan (second row in (A)) using a difference map (bottom row in (A)) and thresholds (B) to determine number of wrap arounds in the low-*venc* data. The resulting combined dual-*venc* data set without remaining aliasing artifact is shown in (C). The arrow in the image of the high-*venc* acquisition (A, second row) indicates the direction of rotation.

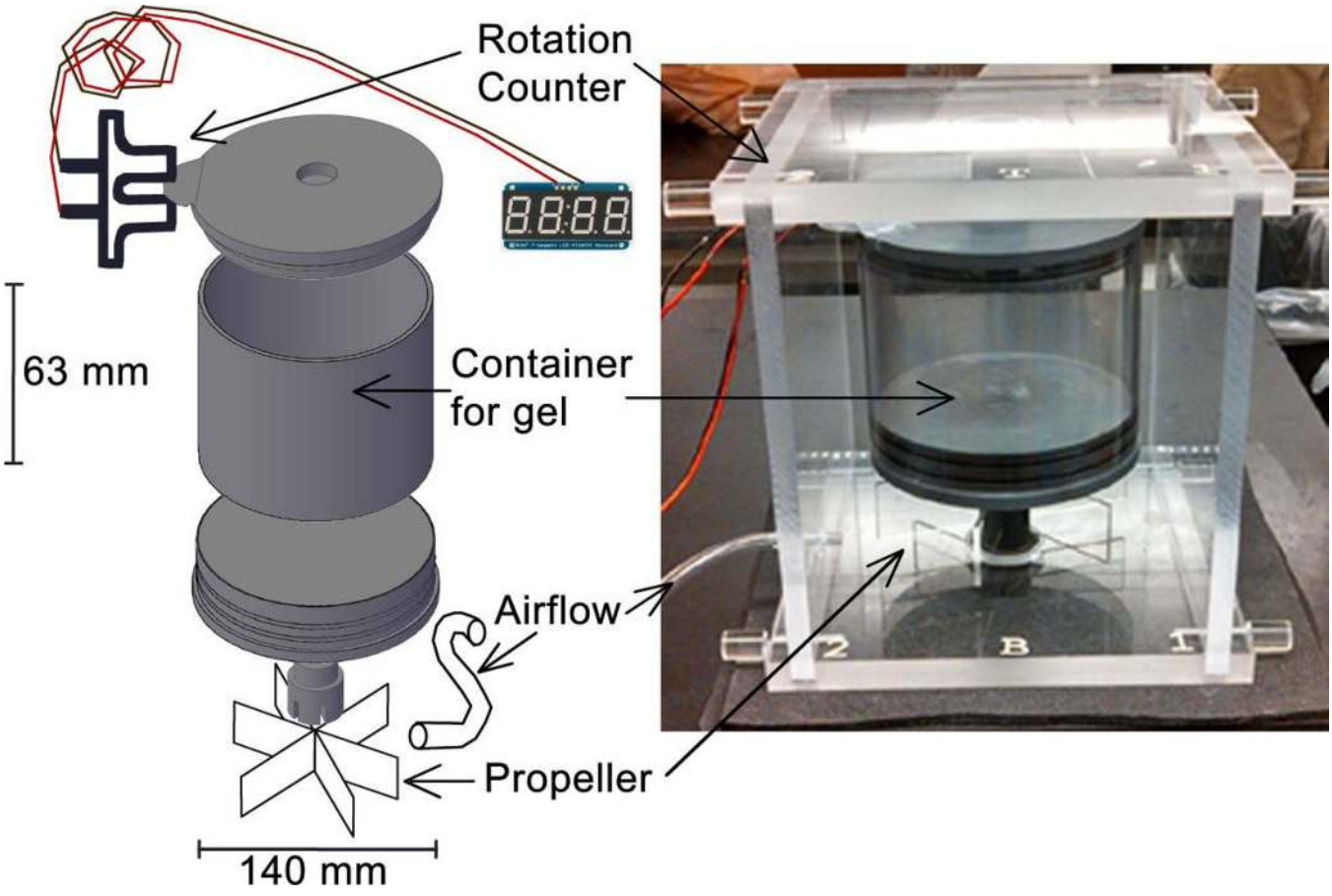

Figure 3.

The rotation phantom consists of a container filled with contrast enhanced media. The container is driven by an air coupled propeller and rotations are counted with a photomicrosensor. Velocities varied linearly from 0 cm/s at the center to a maximum speed of 200 cm/s.

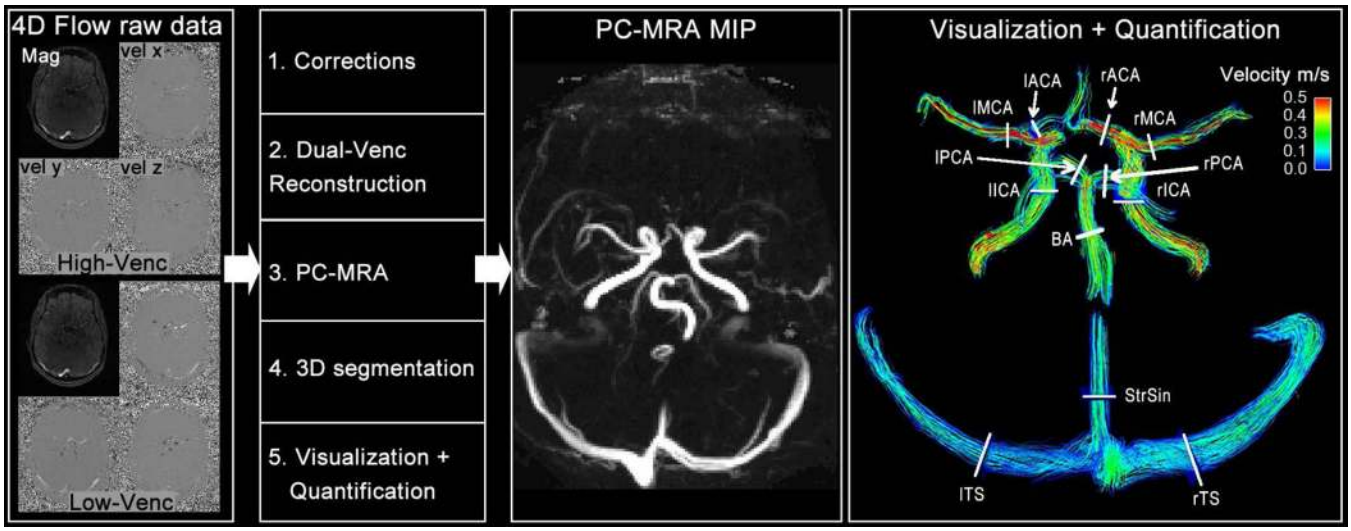

Figure 4.

Magnitude and phase raw data of the low- and high-*venc* (left panel) is used to pre-process, reconstruct the dual-*venc* data set (Figure 3), calculate the PC-MRAs for all three acquisitions: low-, high- and dual-*venc*. The low-*venc* PC-MRA is used to segment the angiogram (MIMICS, Materialize, Belgium). From the PC-MRAs, the maximum intensity projection (MIP) is calculated along all spatial directions (second panel from right depict an axial MIP), which is used for qualitative grading. The segmented angiogram from the low-*venc* acquisition is used to mask velocities in all three data sets in order to get precise quantification of peak velocity and net flow at all defined locations (right panel): left and right internal carotid artery (lICA + rICA), left and right middle cerebral artery (lMCA + rMCA), left and right anterior cerebral artery (lACA + rACA), left and right posterior cerebral artery (lPCA + rPCA), basilar artery (BA), left and right transverse sinus (lTS + rTS) and straight sinus. The angiogram mask is also used to restrict the streamlines to the vessel boundaries for visualization of intracranial blood flow (right panel depicts streamlines at peak systole).

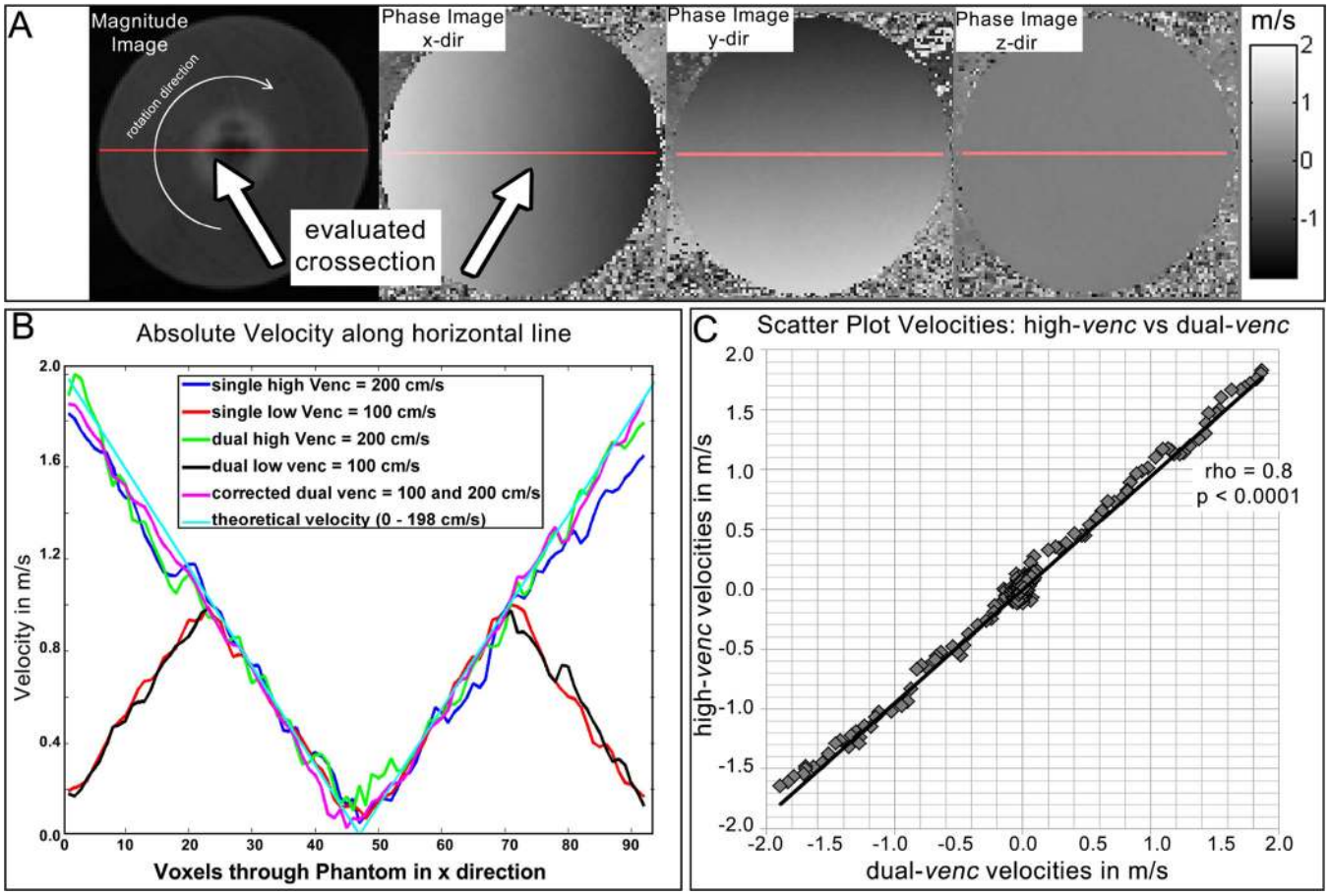

Figure 5.

A. Magnitude and corresponding phase difference images of the rotation phantom in an axial cut plane. The cross section through the center of the phantom used for velocity quantification is shown by the red line. The arrow in the magnitude image indicates the direction of rotation. B. measured absolute along the cross section. The blue and green curves represent the high-*venc* scans measured with a *venc* of 200 cm/s, and the red and black lines represent the low-*venc* scans with aliasing at the outer voxels (*venc* = 100 cm/s). The magenta line represents the combined data set (dual-*venc* corrected scan) showing the result after dual-*venc* reconstruction. The cyan line corresponds to the calculated velocity assuming 198 cm/s at the outer diameter at 4.5 rev/s. C. Correlation of absolute velocities along the horizontal line for dual- vs high-*venc* shows a significant Spearman rank sum correlation of $\rho = 0.8$, indicating successful velocity anti-aliasing by dual-*venc* reconstruction.

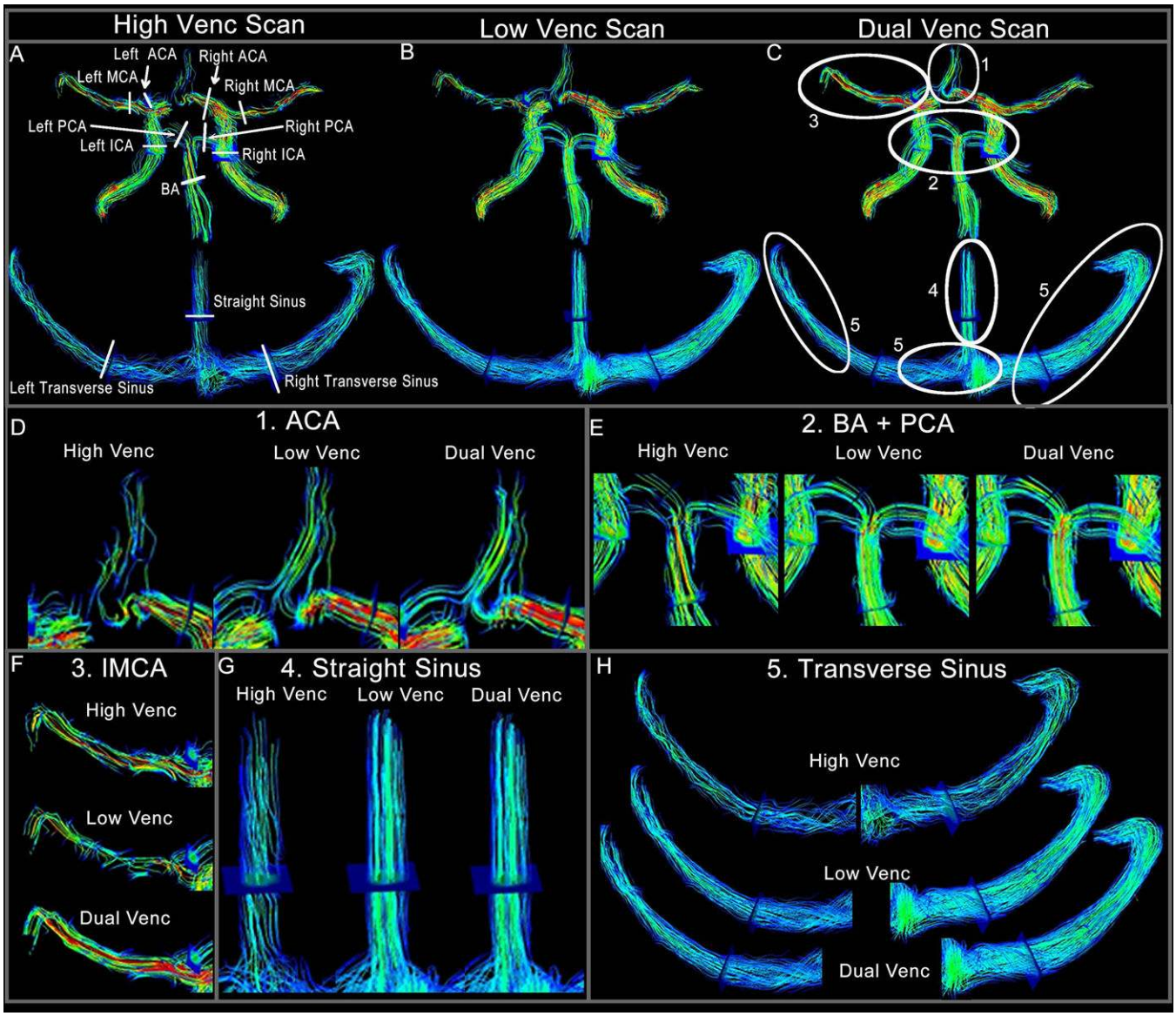

Figure 6.

Panels A–C show an example of one volunteer with 3D streamlines emitted from the entire angiogram volume for all three 4D flow scans (A high-*venc*, B low-*venc* and C dual-*venc*). The plane locations for flow quantification and quality assessment are illustrated in A. Those planes were also used to determine net flow and peak velocity. In panels D–H the areas in which dual-*venc* 4D-flow MRI provided superior flow visualization are zoomed. Panel D shows more as well as more coherent streamlines for the ACA. Panel E shows the BA and PCA, panel F shows disrupted streamlines in the low-*venc*, which are corrected in the dual-venc and panels G and E show examples of the slow flow venous system.

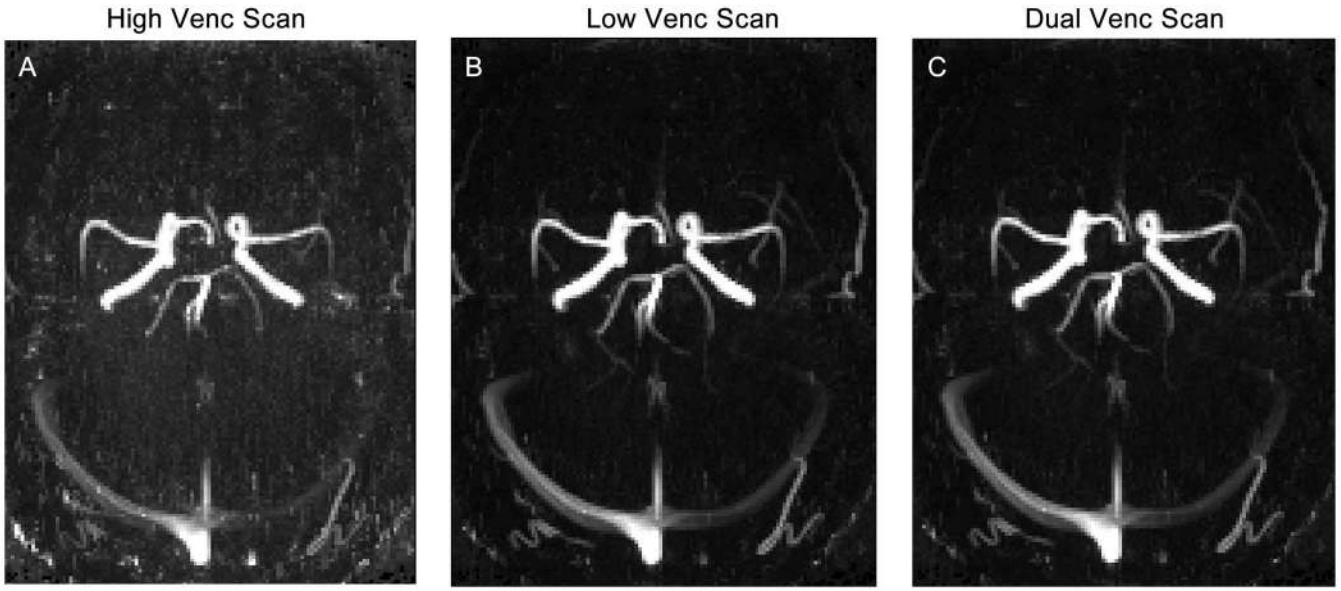

Figure 7.
Example of the PC-MRA MIP for one volunteer, in A high-*venc*, B low-*venc* and C dual-*venc*.

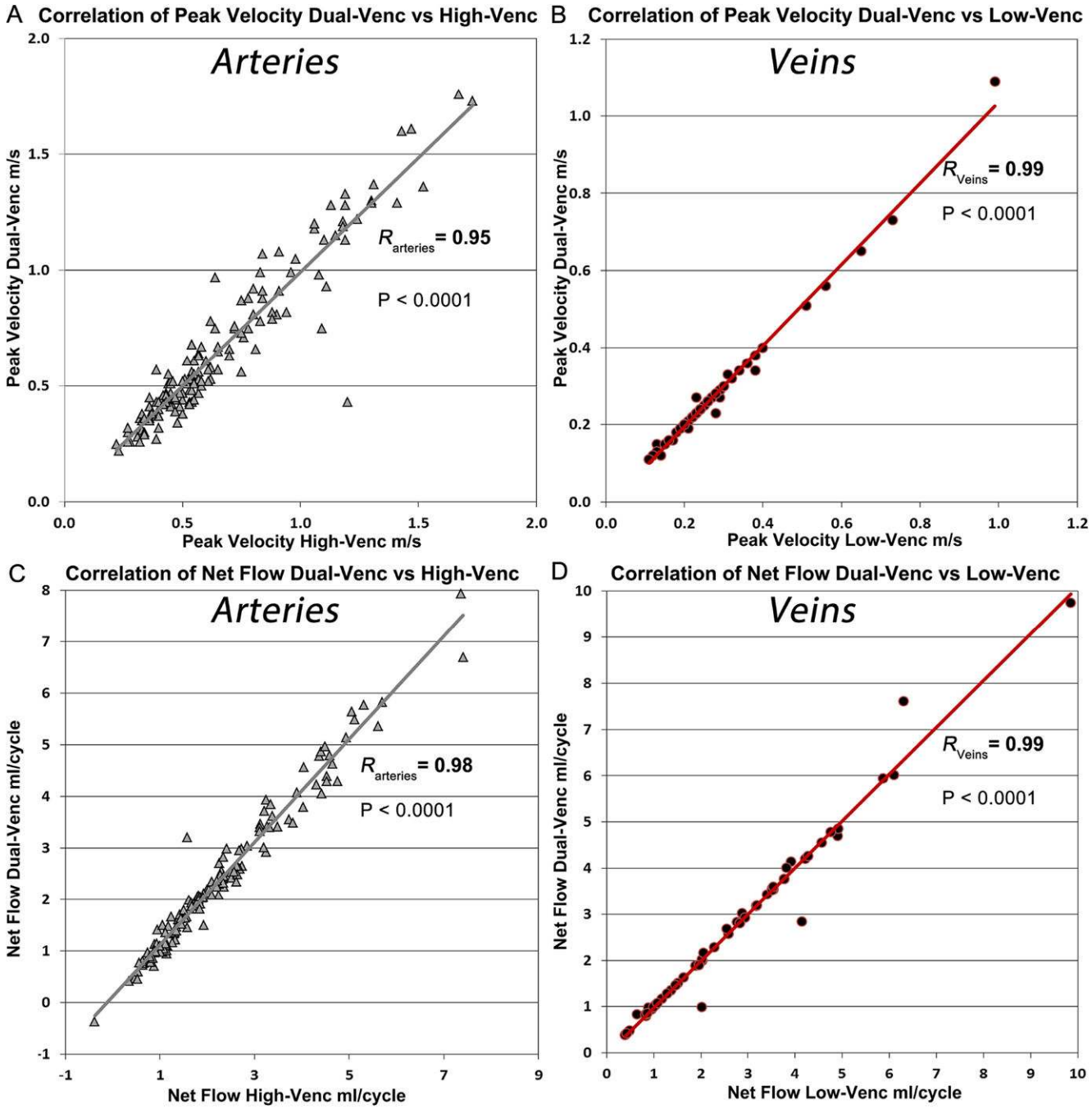

Figure 8.

The grey line depicts the correlation of peak velocity of dual-*venc* with high-*venc* (A) and the red line the correlation of dual-*venc* with low *venc* (B). (C) Correlation of net flow of dual-*venc* vs high-*venc* depicted with grey line. (D) Correlation of net flow dual-*venc* vs low-*venc* depicted with red line. *R* = Pearson correlation coefficient of the correlation.

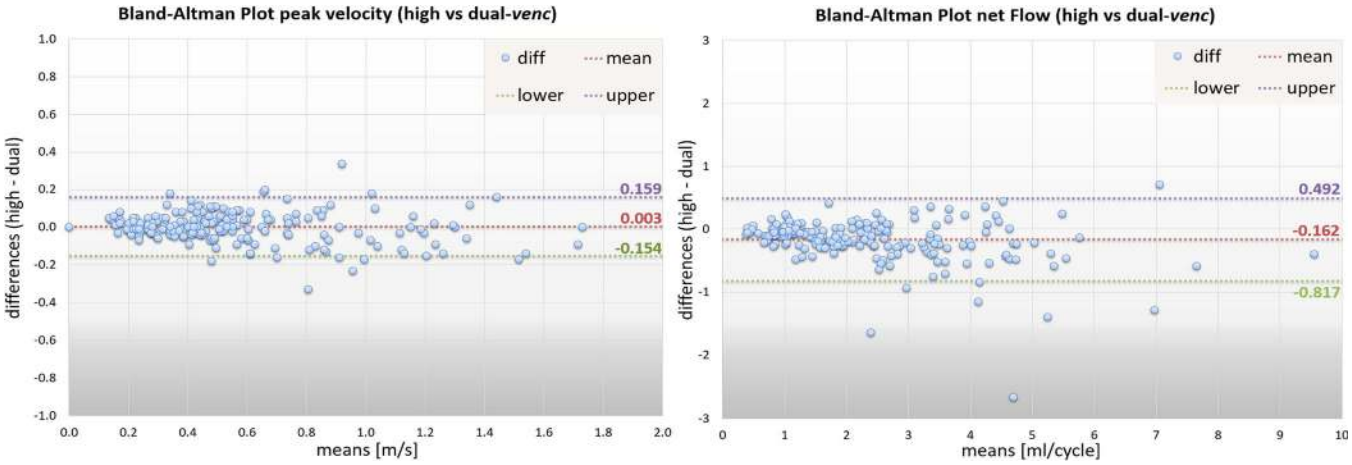

Figure 9.

Bland-Altman plots for peak velocity values in all vessels (left panel) as well as net flow values in all vessels (right panel) between the high- and dual-*venc* acquisitions.

Table 1

Results of Quality Grading for Vessel Depiction (summed up for all 15 locations, 0 = not present, 1 = partly/incomplete, 2 = clear/complete), Noise (mild = 0, moderate = 1, severe = 2) and Artifact impression (mild = 0, moderate = 1, severe = 2).

	Vessel Depiction			Noise Impression			Artifact Impression		
	High-Venc	**Low-Venc**	**Dual-Venc**	**High-Venc**	**Low-Venc**	**Dual-Venc**	**High-Venc**	**Low-Venc**	**Dual-Venc**
Mean ± Std	20.2 ± 3.2	27.0 ± 1.6	27.2 ± 1.5	1.6 ± 1.5	0.5 ± 0.5	0.3 ± 0.3	0.8 ± 1	0.3 ± 0	0.1 ± 0
median	21	27	27	1.5	0.5	0.5	1	0	0
$P_{low\_vs\_dual}$		0.3750			0.0156			0.1875	
$P_{high\_vs\_dual}$		< 0.0001			< 0.0001			< 0.0001	
$P_{high\_vs\_low}$		< 0.0001			< 0.0001			0.0067	